

Nanostructural Analysis of Co-Re/ γ -Al₂O₃ Fischer-Tropsch Catalyst by TEM and XRD

Roya Dehghan-Niri,^[a, b] Nikolaos E. Tsakoumis,^[c, d] Alexey Voronov,^[d, e] Anders Holmen,^[d] Randi Holmestad,^[a] Per-Erik Vullum,^[a, f] Øyvind Borg,^[b] Erling. Rytter,^[b, d] Magnus. Rønning,^[d] and John C. Walmsley^{*[a, f, g]}

A rhenium promoted Fischer-Tropsch (FT) cobalt catalyst supported on γ -Al₂O₃ has been investigated by Transmission Electron Microscopy (TEM) and X-ray Diffraction (XRD), before and after reduction. Electron diffraction, High Resolution TEM and Electron Energy Loss Spectroscopy were used to confirm the oxidation state. Cobalt aggregate, particle and crystallite sizes have been studied in detail and measured by TEM and XRD. A cobalt particle size of 10.0 ± 2.4 nm obtained from bright field TEM images for the reduced material is consistent with the

XRD analysis of the calcined catalyst. After reduction dark field TEM imaging gave a volume-weighted crystallite size of 7.5 ± 2.5 nm, which is close to the value obtained by XRD. The particles had lost the parallel orientation and physical continuity within the alumina pore structure that were present before reduction. The latter was confirmed by electron tomography. Lamellae identified with the presence of Hexagonal Close Packed cobalt were observed in the predominantly Face Centred Cubic particles.

Introduction

Cobalt supported on alumina is one of the main catalysts for the Fischer-Tropsch (FT) process that is used to convert synthesis gas into fuels.^[1,2] The efficiency of the catalytic reaction depends on the number of cobalt atoms deposited on the surface of the substrate in the form of metallic nano-

particles, that are exposed to the gaseous reactants.^[1] To be able to improve the efficiency of the reaction, the structure of the catalysts must be understood at the nanometre scale. Transmission Electron Microscopy (TEM) and X-ray Diffraction (XRD) are two powerful characterization techniques that provide complementary information on the cobalt nanoparticles. TEM provides direct imaging of a very limited region of the sample in which the dispersion, particle morphology, and crystallographic phases can be distinguished. XRD provides structural information from the bulk material and is able to give an average picture of the phases that are present in the sample and of the average crystallite size. It is generally more convenient to study these catalysts by XRD and TEM after calcination, in their oxide state. There are few studies using TEM to characterize the reduced cobalt FT catalyst.^[3,4] Here, we compare the catalyst in both oxide and reduced states.

Since TEM probes a local region of the sample, good statistics are required to obtain representative information. TEM provides a two-dimensional projection of a section through a sample, from which individual particle morphology and size can be measured directly to produce a particle-size distribution.

In XRD the average crystallite size are determined through the Scherrer formula, which relates broadening of the Bragg peak to the number of parallel lattice planes that are diffracting.

Metallic cobalt nanoparticles are active in the FT process and cobalt oxide precursors are reduced under H₂. Cobalt oxide (Co₃O₄) has a spinel structure in which the Co²⁺ ions occupy tetrahedral sites and Co³⁺ ions occupy octahedral sites.^[5] As oxygen atoms are eliminated from the Co₃O₄ structure, it is first transformed to cobalt monoxide (CoO), with a Face Centred Cubic (fcc) structure^[1,6,7]

In CoO, the cobalt atoms are located on the corners and the sides of the cubic unit cell, while the oxygen atoms are located on the edges and centre. With further reduction, the CoO is converted to fcc or Hexagonal Close Packed (hcp) metallic

[a] Dr. R. Dehghan-Niri, Prof. R. Holmestad, Dr. P.-E. Vullum, Dr. J. C. Walmsley
Department of Physics
Norwegian University of Science and Technology (NTNU)
7491, Trondheim (Norway)

[b] Dr. R. Dehghan-Niri, Dr. Ø. Borg, Prof. E. Rytter
Equinor Research Centre
7053, Trondheim (Norway)


[c] Dr. N. E. Tsakoumis
SINTEF, Process Technology
7034 Trondheim (Norway)


[d] Dr. N. E. Tsakoumis, Dr. A. Voronov, Prof. A. Holmen, Prof. E. Rytter,
Prof. M. Rønning
Department of Chemical Engineering, NTNU
7491, Trondheim (Norway)

[e] Dr. A. Voronov
Present address:
CJSC "SuperOx"
Nauchny proezd, 20
117246, Moscow (Russia)

[f] Dr. P.-E. Vullum, Dr. J. C. Walmsley
SINTEF, Materials and Chemistry
Høgskoleringen 5
7034 Trondheim (Norway)

[g] Dr. J. C. Walmsley
Present address:
Department of Materials Science and Metallurgy
University of Cambridge
Cambridge, CB30FS (UK)
E-mail: jcw80@cam.ac.uk

 Supporting information for this article is available on the WWW under <https://doi.org/10.1002/cctc.202101931>

 © 2022 The Authors. ChemCatChem published by Wiley-VCH GmbH. This is an open access article under the terms of the Creative Commons Attribution License, which permits use, distribution and reproduction in any medium, provided the original work is properly cited.

cobalt.^[7] The oxygen elimination causes structural shrinkage; 12.2% by volume from Co₃O₄ to CoO, 42.4% from CoO to cubic cobalt and 42.7% from CoO to hexagonal cobalt. Bulk metallic cobalt has an hcp structure at temperatures below 420 °C, while at higher temperatures fcc cobalt is stable.^[8,9] In supported cobalt materials, however, both fcc and hcp cobalt structures have been observed at temperatures below the transition temperature.^[9–11] The cobalt structure is known to be particle-size dependent.^[10–12] Kitakami et al. have reported that cobalt nanoparticles smaller than 20 nm were fcc and those larger than 40 nm were hcp, while particles with a size around 30 nm were a mixture of both fcc and hcp.^[12]

Several studies have been made on the characterization and structural analysis of supported cobalt FT catalysts,^[3,7,10–14] however, some aspects remain unresolved. In particular, detailed observation of the catalyst in the reduced state and the relationship of its nanostructure to its catalytic behaviour is lacking. In our previous work,^[11] cobalt supported on γ -Al₂O₃, a catalyst similar to the one studied here, was studied by TEM; our findings indicated that the cobalt oxide phase is present mostly in mosaic aggregates with parallel crystallographic orientation. The aggregate size was found to be considerably larger than the Co₃O₄ crystallite size measured by X-ray diffraction. For a similar catalyst electron tomography showed that the cobalt oxide filled the pores inside the alumina support and fully interpenetrated the support.^[15] Li et al.^[3] have studied Ru-promoted and non-promoted alumina supported cobalt catalysts after reduction by TEM. In the non-promoted catalysts, they observed the reduction of the Co₃O₄ to the intermediate cubic CoO phase. In contrast, in the promoted catalyst, in addition to the formation of large CoO particles, they detected the formation of either of CoRu or Ru nanoparticles.

In the present study, a 20wt%Co/0.5wt%Re/ γ -Al₂O₃ catalyst is examined before and after reduction by different TEM analysis techniques, such as bright field, dark field, and electron diffraction. Rhenium has been chosen as a reduction promotor due to its positive effect on the selectivity to higher hydrocarbons,^[16–19] while its availability is much higher than other precious metal promoters such as Ru and Pt, a fact that is reflected in the catalyst production cost. Electron diffraction is used to identify the nanoparticle structures. Dark field imaging is used to identify the crystallites sharing a specific crystallographic orientation. Since cobalt nanoparticles are oxidized rapidly on exposure to ambient atmosphere, the reduced material is transferred inertly from a glove box to the TEM. This method has been applied previously to transfer TEM samples of air-sensitive alanate materials.^[20]

XRD is routinely performed on the calcined catalyst before reduction. However, there are some in-situ XRD studies in which the microstructure of reduced cobalt catalyst supported on alumina has been investigated.^[9,10,14,21,22] In all of these studies, both fcc and hcp cobalt were observed after H₂ reduction and fcc was the dominant metallic phase. Ducreux et al.^[9] have studied Co/Al₂O₃ catalyst and concluded that the metallic phase after reduction is a mixture of fcc and hcp in a defective structure, rather than being a mixture of single-phase particles, with a high density of fcc/hcp stacking faults. They showed that

the degree to which the defects are present is related to the reduction temperature. For a low reduction temperature, hcp was the dominant structure and it contained fcc stacking faults. At a higher reduction temperature, an fcc structure was observed in which hcp faults were present. They found that the hcp particles with higher stacking fault densities have higher activity and that the modification of the cobalt structure to hcp can be achieved by carbide formation under CO gas and its subsequent decomposition under H₂. Since the carbide decomposition takes place at lower temperature, it favours the formation of hcp cobalt.^[9,12] However, this route suffers from carbon formation on the catalyst that can severely affect catalytic performance.^[23]

Results

The results of the TEM and XRD experiments are described in the following paragraphs.

Two Dimensional TEM Analysis

Figure 1a shows a TEM image of the cobalt oxide catalyst at low magnification in the sample prepared by ultramicrotomy. The cobalt oxide aggregates are the dark areas appearing on the bright background, which is the alumina support. Some of the cobalt oxide aggregates are indicated by arrows. The aggregate size was measured at several positions in the sample. As seen in Figure 1b, the aggregate size varies from small aggregates, in the diameter range of 70–90 nm, to large aggregates in the range of 200–250 nm and the majority are in the range of 100–150 nm. The measurements give an average of 150 ± 30 nm. In ultramicrotomy samples, it is not possible to distinguish the aggregates cut through the centre, meaning that the average size will be underestimated. To compensate for this, a correction was applied^[24] and the obtained average aggregate diameter was 158 ± 30 nm.

Figure 2 shows detailed TEM images of the catalyst before reduction. Figure 2a is a bright field image showing a few cobalt aggregates on the alumina substrate. Figure 2b is the diffraction pattern of the large cobalt oxide aggregate.

The continuous rings in the diffraction pattern are from the alumina phase, which has low crystallinity, and the strong diffraction spots are from the crystalline cobalt oxide phases. The sample has been tilted so that an aggregate at the centre of the field of view is oriented to a [110] zone axis orientation. Figure 2c is a dark field image from the same area as in Figure 2a, formed from a {111} Co₃O₄ reflection. Table 1 shows the principle inter-planar spacings of the main phases which can be present in the catalysts. As seen in Table 1, γ -Al₂O₃ and cobalt phases have some *d* values close to each other. In order to distinguish between γ -Al₂O₃ and cobalt phases in dark field images, hollow-cone imaging was applied. In Figure 2d, the dark field angle of tilt has been made larger than that of the main reflections from the catalyst and support phases.^[25,26] In this image, diffraction contrast is suppressed and the Co₃O₄,

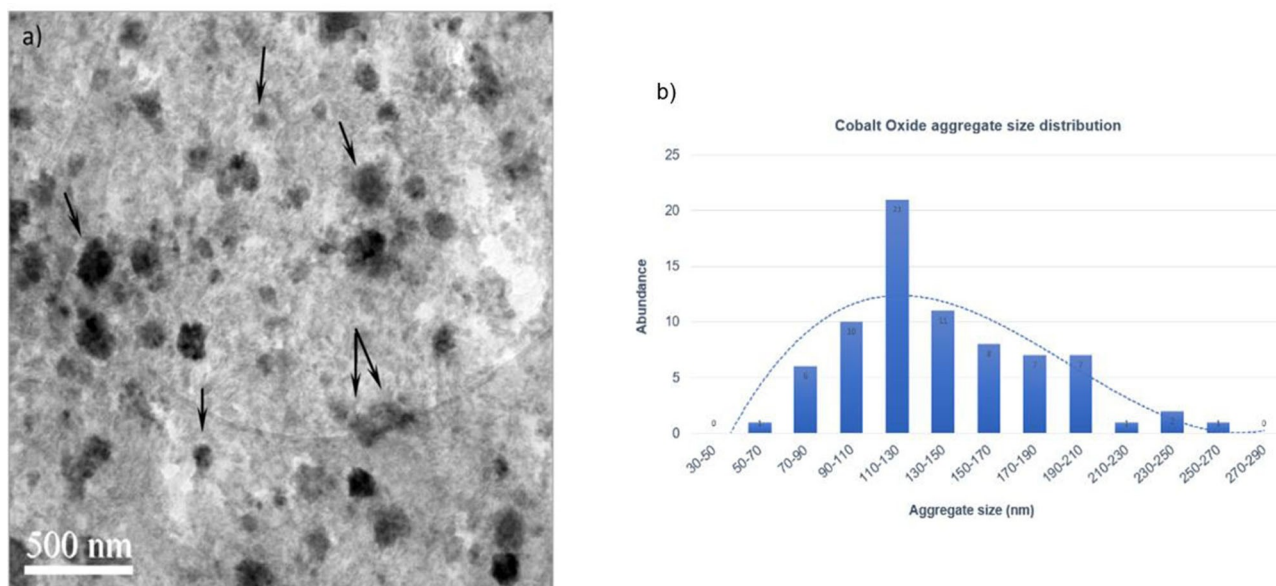


Figure 1. 1 a) TEM image of catalysts, samples prepared by ultramicrotomy, 1 b). The cobalt oxide aggregate size histogram with 20 nm bin size.

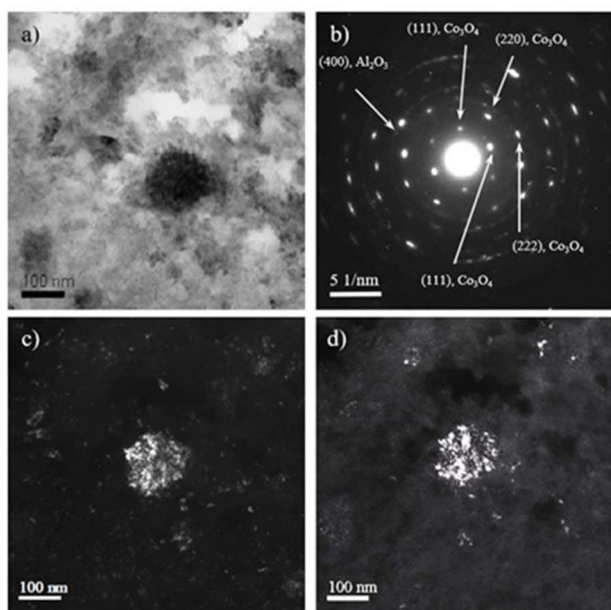


Figure 2. 2 a) Bright field TEM image of cobalt oxide aggregate supported on alumina, 2 b). diffraction pattern of centered aggregate, 2 c). Dark field image of same area from (111) reflection, 2 d). Conical dark field in which the alumina diffraction rings have been avoided.

Table 1. Different main d values of components of the catalyst.				
Co (H) Hexagonal [Å]	Co (C) Cubic [Å]	CoO (C) Cubic [Å]	Al ₂ O ₃ (C) Cubic [Å]	Re (H) Hexagonal [Å]
2.16(100)	2.05(111)	2.46(111)	4.56(111)	2.38(100)
2.02(002)	1.77(200)	2.13(200)	2.39(311)	2.23(100)
1.91(101)	1.25(220)	1.51(220)	2.28(222)	2.10(101)
1.25(110)	1.06(311)	1.28(311)	1.97(400)	1.38(110)
1.15(103)	1.02(222)	1.23(222)	1.39(440)	1.17(112)

which has a higher atomic number than the support, appears brighter. At the same time, diffraction contrast from crystallites in the support is lost. This confirms that most of the cobalt is located in the aggregates with smaller amounts of cobalt being distributed in the support between them.

The γ -Al₂O₃ substrate, without any cobalt precursor, was also analysed in order to explore the diffraction contrast from the support. A series of bright field, dark field and diffraction pattern has been acquired from this material. Figure 3 shows the diffraction pattern from this series. Corresponding bright field images showed low contrast that is consistent with the low crystallinity of the support. However, dark field images

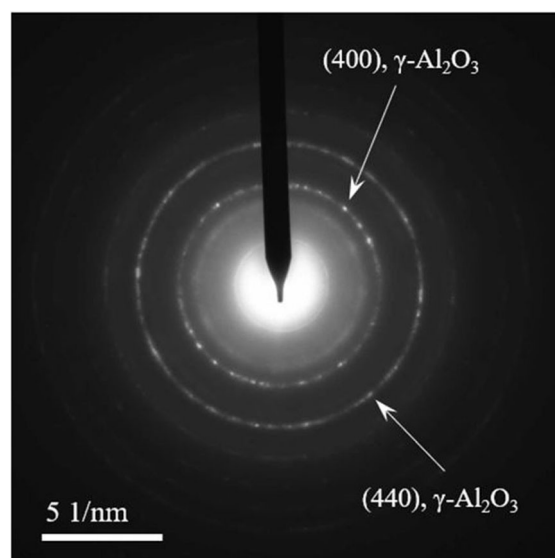


Figure 3. Diffraction pattern of γ -Al₂O₃ material without cobalt phase.

produced by the {400} alumina planes, with normalized contrast show significant contrast from some of the alumina crystallites. As this spacing is close to that of the Co-containing phases, this indicates that some of the smaller features showing contrast in the catalyst loaded sample were from the substrate. In order to estimate the accuracy of lattice parameter measurements and to calibrate the diffraction pattern measurements, a clean Al_2O_3 ring pattern was used. The d_{400} values of about 20 different distinct crystallites spots on the ring were measured precisely and an average value of $1.97 \pm 0.03 \text{ \AA}$ was obtained. This is important when considering individual cobalt particles as it is difficult to distinguish between some of the Co_3O_4 and Co hcp/fcc spacings. For instance, a value of 2.02 \AA could be from {400} Co_3O_4 planes, from {002} hcp Co planes or from {111} fcc Co planes, Table 1. It is important to note that there are other spacings for the oxide or metallic structures that are well separated from the spacings of other phases, so that it is possible to judge when a sample has been fully reduced.

The changes in the aggregates on reduction are well illustrated in Figure 4, a high resolution TEM image of a cobalt oxide aggregate. It is oriented so that {200} planes are in contrast. No separate, individual, cobalt oxide particles can be distinguished, and the lattice fringes are continuous across the entire aggregate. This is demonstrated by the inset Fourier transform taken from the whole of the image and the local detail of the lattice fringes from the Co_3O_4 aggregate. The aggregate is significantly larger than the pore size of the support.

By comparison, Figure 4b shows a bright field image of a cobalt aggregate after reduction. Individual cobalt particles are now readily distinguished. Furthermore, stacking-fault-type contrast is present within the particles. The latter shows

irregular orientations with respect to each other, further suggesting that the particles have different orientations.

Figure 5 shows bright field and dark field images as well as the corresponding diffraction pattern of the catalyst after reduction. The spots indicated on Figure 5c show d values of 2.05 \AA and 1.91 \AA , which correspond to cobalt fcc {111} planes and cobalt hcp {101} planes, respectively. As measurements are made on the same negative, accurate relative values are obtained. None of the distinct reflections from Co_3O_4 were present. Only weak intensity related to CoO {200} planes was observed in the diffraction patterns, suggesting a high degree of cobalt reduction. The presence of metallic cobalt has been further confirmed by Electron Energy Loss Spectroscopy (EELS). Figure 6a shows the image of a reduced cobalt aggregate obtained by STEM and Figure 6b is the EELS spectrum from an indicated cobalt nanoparticle. In the spectrum only the Co-L_{2,3} edge is present; the O-K edge at 532 eV is not visible, confirming that the cobalt nanoparticle is in metallic state. Comparing the diffraction pattern from only the alumina substrate (Figure 3) with the diffraction pattern from the reduced catalyst (Figure 5c) indicates that some weak reflections from fcc cobalt can be seen at different positions within the {400} alumina ring in other orientations. According to the data in Table 1, the d values corresponding to the strongest reflections of both hexagonal and cubic cobalt are close to the {400} reflections of alumina. It is not possible to separate the intensity of alumina from these cobalt reflections with the smallest objective aperture to obtain a dark field image only from the cobalt phase. The dark field in Figure 5b is produced by a {111} fcc reflection and it shows the distribution of {111} fcc crystallites in the aggregate.

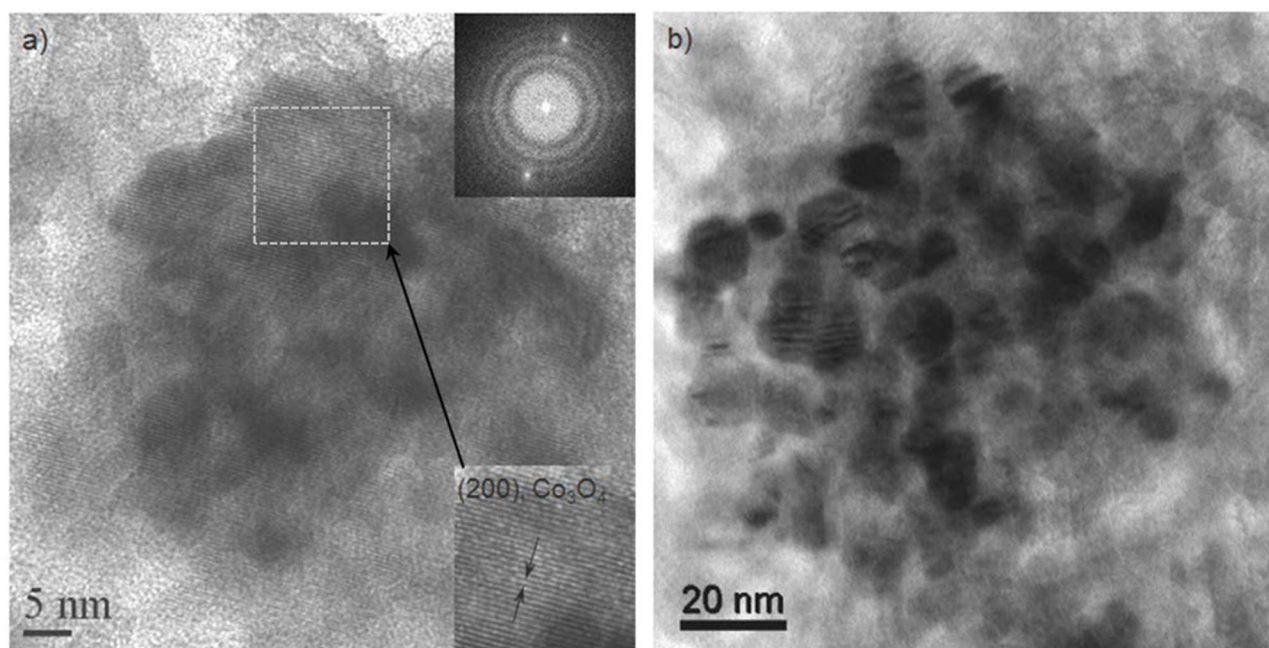


Figure 4. 4a High Resolution TEM image of cobalt oxide aggregate, 4b. Bright field TEM image of a similar reduced cobalt aggregate.

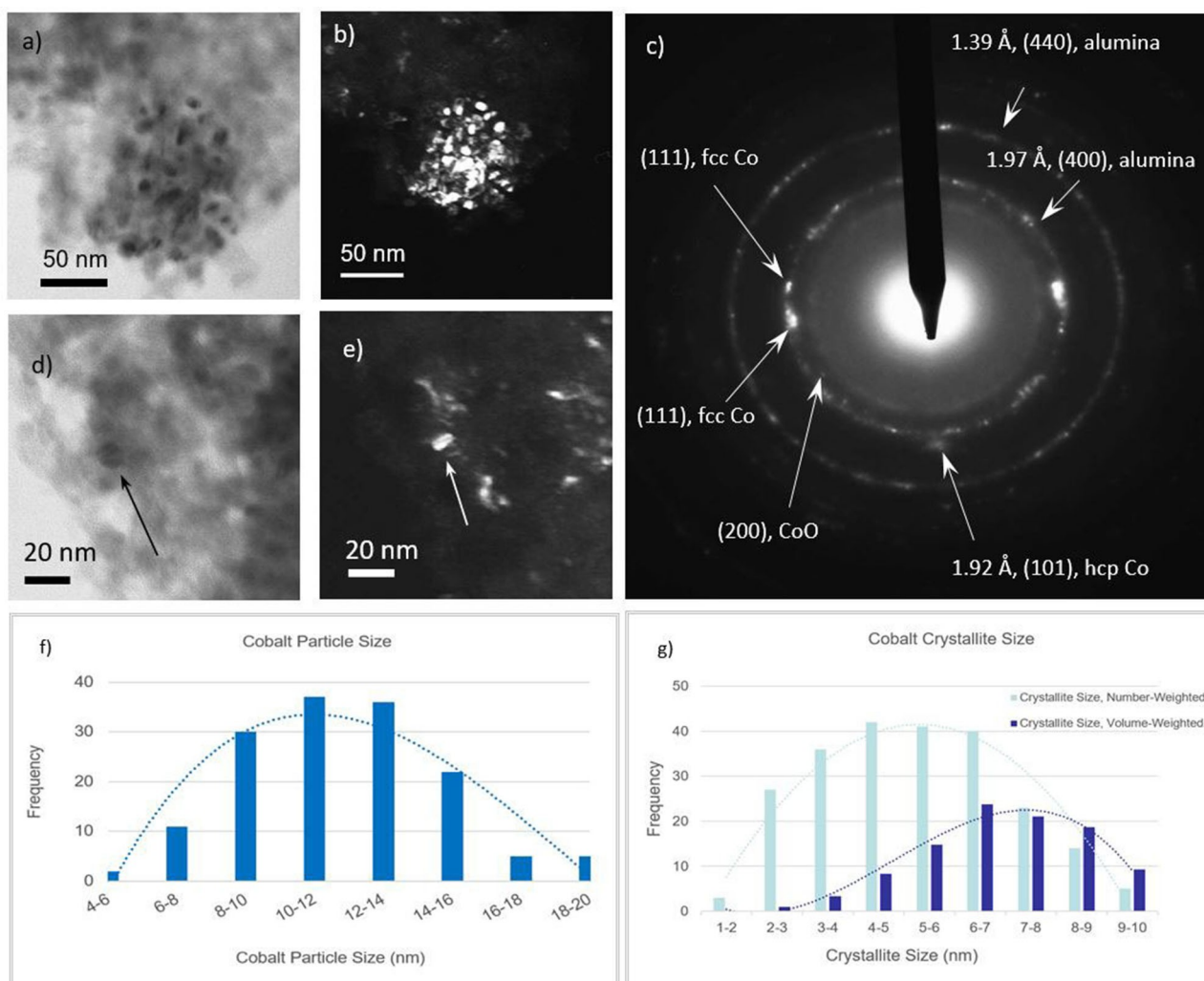


Figure 5. **5a** Bright field TEM image of reduced 20%Co/0.5%Re/γ-Al₂O₃, **5b** Dark field image of the same area generated by (111) reflections of fcc cobalt, **5c** Diffraction pattern of same area, **5d** Bright field image of a cobalt nanoparticle containing two different crystallite and **5e** its related dark field image, **5f** Particle size distribution measured on bright field images, **5g** Crystallite size histograms measured on dark field images with polynomial fit, showing both number-weighted and volume weighted crystallite size distribution.

Figures 5d and 5e are bright field and corresponding dark field images of a cobalt particle, respectively. Comparison of these images shows that only part of the particle has contrast in the dark field image and the particle size in the bright field image is larger than in the dark field image. This indicates that more than one crystal orientations are present in the particle.

Figures 5f and 5g show the size distributions of the cobalt particles and cobalt crystallites, which were measured from bright field and dark field images, respectively.

The cobalt particle sizes were averaged over about 150 particles measured on several bright field TEM images and gave the value of 10.0 ± 2.4 nm. The crystallite sizes were averaged on about 200 crystallites from different dark field images and the obtained value was 5.3 ± 1.8 nm. Particle size measurements from TEM images are based on the number of particles with the same group size with 1 nm bin size. In order to make the TEM results comparable with XRD measurements which are volume based, a volume factor has been included into the

measurements.^[27,28] The average volume-weighted crystallite size from TEM observations is 7.5 ± 2.5 nm.

The cobalt aggregate size was measured after reduction, and it gave an average value of 145 ± 40 nm. The aggregate size measurements in the reduced material performed on the TEM sample prepared by dispersion of crushed catalyst powder, not microtomy slices.

Figure 7 shows planar defects in the metallic cobalt aggregates. Figure 7a shows a large cobalt particle, around 20 nm in size. The fringes show the d value of 1.93 Å, which is consistent with the {101} planes of hcp cobalt. Figure 7b shows the existence of hcp lamellae in an fcc cobalt particle. In this particle, the lattice fringe spacings corresponding with {101} hcp and {200} fcc cobalt planes, were measured.

On close examination, most of the cobalt particles were found to contain planar defects. In order to confirm this, the sample was studied by tilting in the range of ± 25 degrees. Figure 8a shows TEM images of the reduced catalyst showing a

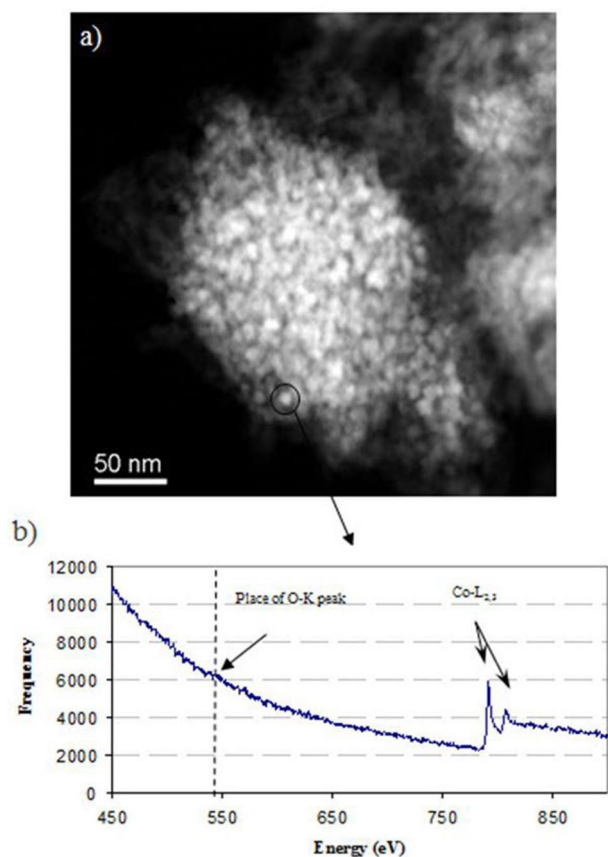


Figure 6. a) STEM image of Re promoted cobalt aggregate supported on γ - Al_2O_3 , b) EELS spectrum of cobalt phase from the indicated position, confirming the presence of only cobalt metal.

few cobalt nanoparticles after tilting the sample by ~ 9 degrees. The defect contrast becomes visible in the cobalt nanoparticles which did not show any contrast at other orientations.

The corresponding non-promoted catalyst was also analyzed to look for the presence of the defects in the cobalt nanoparticles in the absence of promoter. Figure 8b shows the TEM image of the cobalt aggregate from the 20wt%Co/ γ - Al_2O_3 catalyst and defects similar to those in the Re promoted catalyst are present. Some of the faulted cobalt nanoparticles are indicated by arrows.

Three-dimensional TEM Analysis

Figure 9a shows a section through the reconstruction of an electron tomography series of the reduced promoted catalyst. The corresponding movie is available in the following link: (See supporting information movie 1). The tilt series was acquired with a large field of view ($\sim 1 \mu\text{m}$) in order to show several aggregates. As a result, the pixel size in Figure 9b, which is an enlarged view of an aggregate indicated in Figure 9a, is quite large. However, the separation of the particles due to reduction is clearly seen in Figure 9b. The movie of the reconstructed aggregate is available at the following link: (See supporting

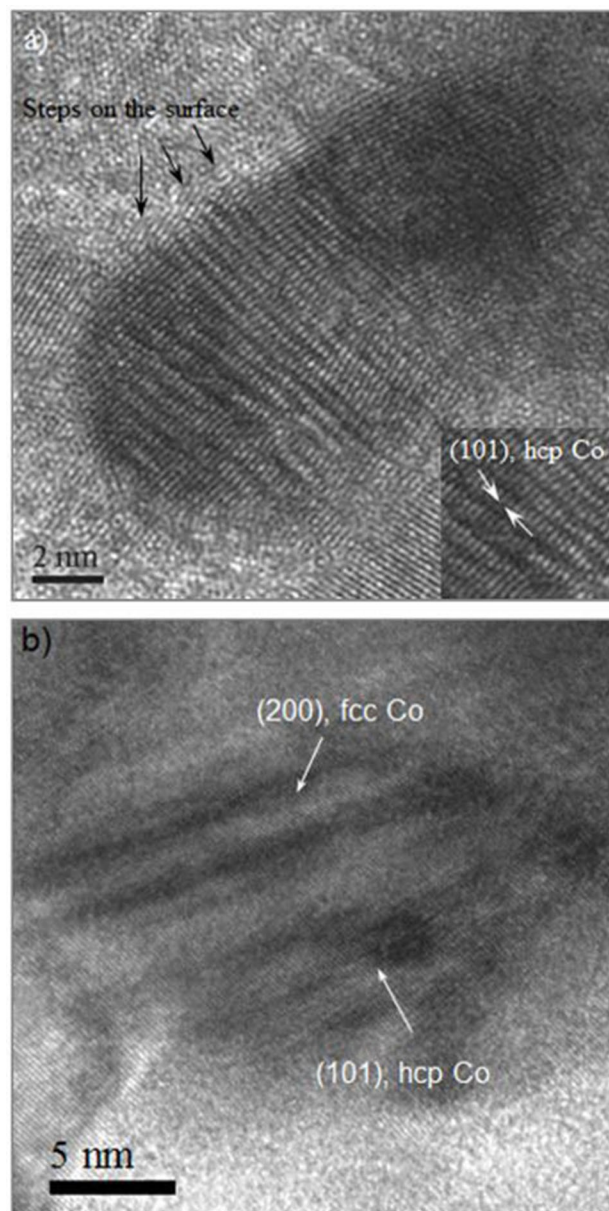


Figure 7. a) Stacking faults in a hcp cobalt particle, b) Presence of fcc lamellae in a hcp cobalt particle.

information movie 2). Figure 9c shows the image after segmentation of the cobalt aggregate through the 3D volume and the following link shows the movie of segmented cobalt aggregate: (See supporting information movie 3).

Tomography shows the details of the distribution of the cobalt nanoparticles in the aggregate. Most show some elongation along different directions, which reflects the influence of pore size and shape of the alumina support on the cobalt phase growth. It should be mentioned that, due to the high contrast in the acquired 3D series, it was difficult to distinguish the boundary of cobalt nanoparticles, which are very closely separated. Hence, some of the large cobalt nanoparticles observed in the segmented 3D views can be groupings of smaller adjacent nanoparticles. The strong contrast between

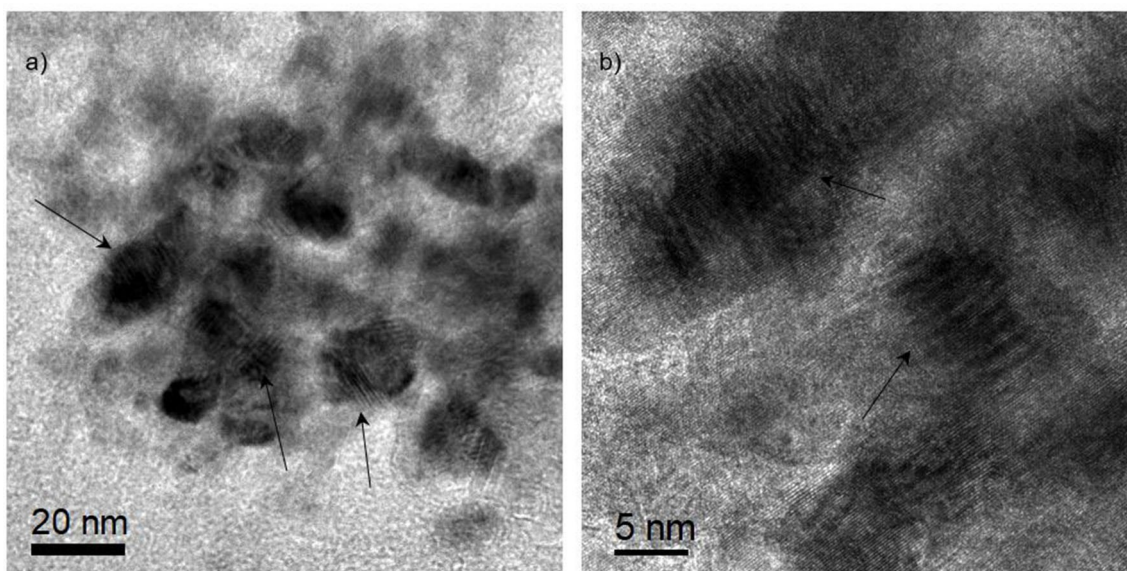


Figure 8. 8a TEM image of promoted catalyst at 9 degree tilt and 8b. Bright field TEM image of reduced 20%Co/Al₂O₃. Arrows indicate faulted particles.

cobalt and support is strongly enhanced in the reconstruction. Figure 9a clearly shows that the cobalt is mostly located in the aggregates with a small number of isolated particles being distributed in the support.

XRD Results

Figure 10 shows the XRD patterns of the catalyst before and after reduction. Figure 10a is the pattern before reduction, in which the presence of spinel cobalt oxide (Co₃O₄) and γ -Al₂O₃ can be observed. Full pattern decomposition was applied and the average crystallite size of the calcined material was calculated by using the mean FWHM (Full Width at Half Maximum) as an input to Scherrer equation. The Co₃O₄ crystallite had an average value of 13.2 ± 1 nm and the γ -Al₂O₃ had 6 ± 1 nm. Figure 10b shows the pattern of the catalyst after reduction. Pattern fitting using pure fcc and hcp crystalline domains fails to completely describe the data, suggesting the existence of defects in accordance with the current TEM results and previous XRD reports.^[9] Both fcc and hcp metallic cobalt phases are detected, with the first being the dominating phase. Line broadening analysis of the XRD peaks gave the average of 5 ± 1 nm for the fcc cobalt crystallites. Table 2 summarizes all

the cobalt nanoparticle and crystallite measurements by TEM and XRD.

Hydrogen Chemisorption Results

Hydrogen chemisorption was performed on the reduced catalyst powder. The amount of adsorbed hydrogen was used to calculate cobalt dispersion and particle size, assuming that two cobalt sites are covered by one hydrogen molecule^[29] and that rhenium does not contribute to the amount of hydrogen adsorbed.

Hydrogen chemisorption characterization of the sample has been reported previously.^[30,31] The type of alumina support for this catalyst is Puralox which matches sample C10 in summarized report by Rytter. et al^[26] indicating particle size of 10.2 nm for this catalyst.^[26]

Discussion

The particle size changes, phase transformations and structural changes are discussed based on the TEM and XRD results.

Table 2. List of TEM and XRD measurements on Co nanoparticles in both oxide and reduced states.			
List of the measurements	State of the material	TEM (Number-weighted) [nm]	XRD (Volume-Weighted) [nm]
Cobalt oxide aggregate size	Calcined	158 ± 30 nm	–
Cobalt oxide crystallite size	Calcined	–	13.2 ± 1 nm
Cobalt aggregate size	Reduced	145 ± 40 nm	–
Cobalt particle size	Reduced	10.0 ± 2.4 nm (Bright field images)	–
Cobalt crystallite size	Reduced	7.5 ± 2.5 nm (Dark field images)	5 ± 1 nm for fcc cobalt

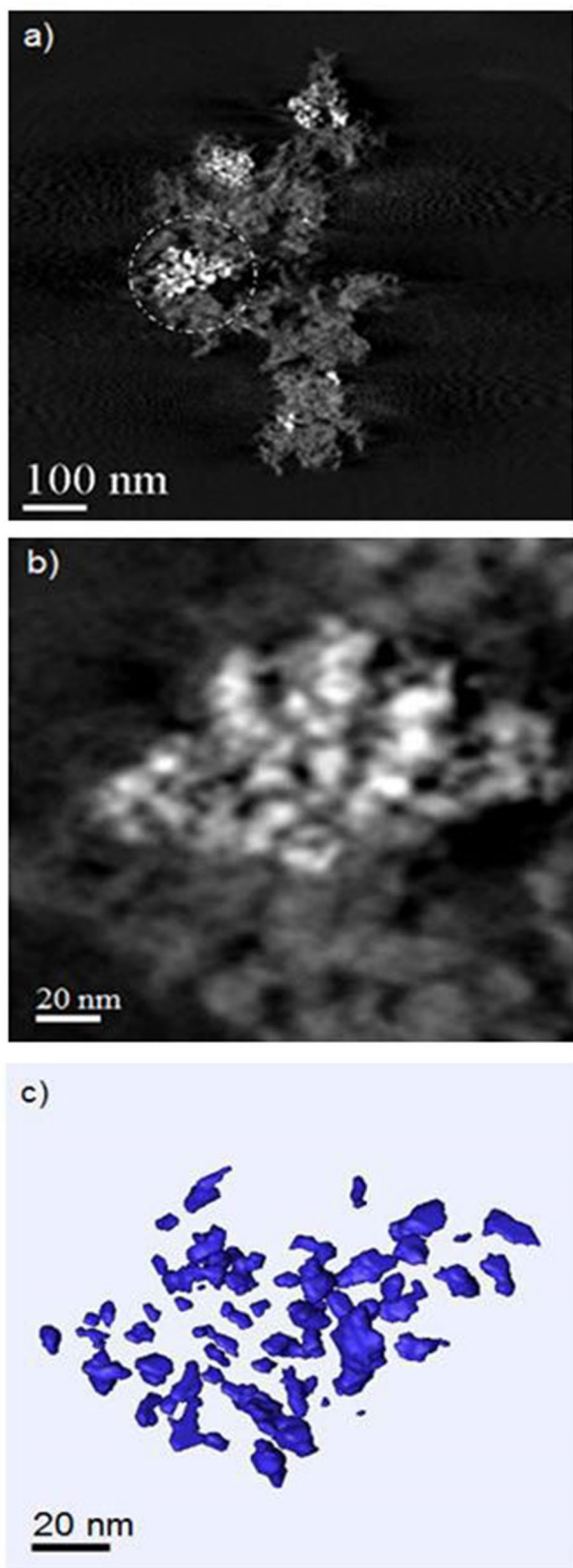


Figure 9. 9a A section through 3D reconstruction of the reduced Re promoted cobalt supported on γ - Al_2O_3 catalyst, 9b. An enlargement of a section through the reconstruction of an indicated aggregate, 9c. Segmentation of the cobalt area.

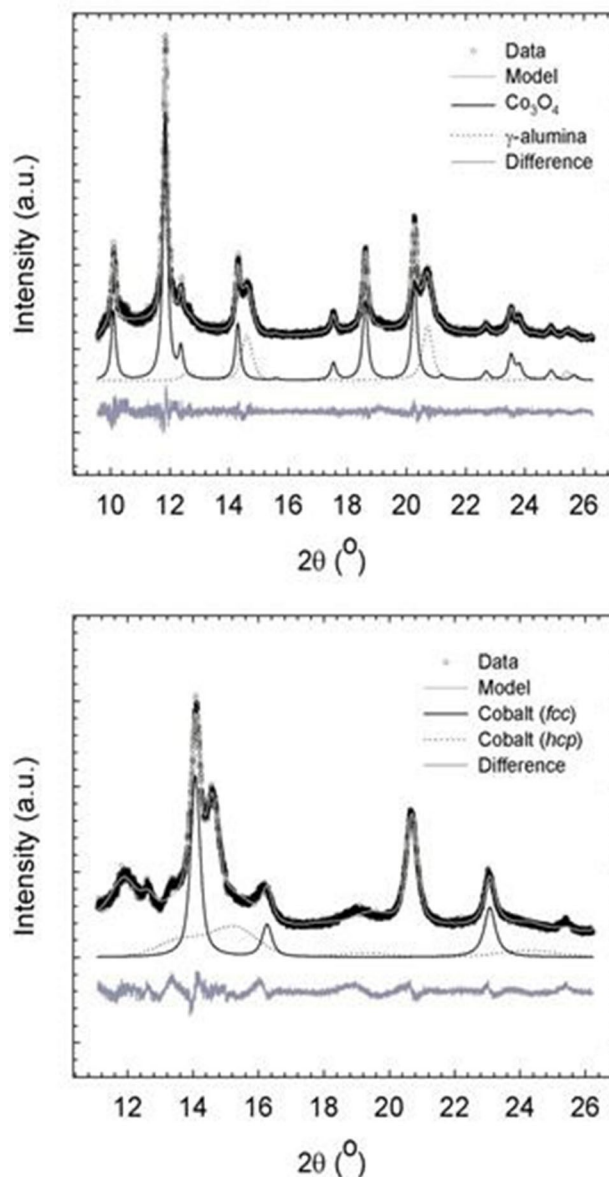


Figure 10. 10a XRD pattern of calcined catalyst before reduction and 10b. XRD pattern of the reduced catalyst after in-situ reduction.

Aggregate/Particle and Crystallite Size Measurements of the Cobalt Phase

The aggregate size measurements using the TEM images, such as Figure 1a, give an average aggregate size around 158 ± 30 nm, after correction. The individual cobalt oxide crystallites produced through the calcination process have an average size of 13.2 ± 1 nm, according to the XRD results. This means that each aggregate contains many agglomerated cobalt oxide crystallites. This is consistent with our earlier observations.^[13] The agglomeration of particles causes difficulties in TEM imaging of the individual particles and, consequently, the size determination. Although a few individual oxide particles could be observed, it is not possible to extrapolate their size to a

sample as a whole. However, XRD effectively measures the bulk of the calcined material and gives the average crystallite size.

The TEM analysis of the reduced samples indicates that the cobalt aggregates keep their overall shape and size from before the reduction and that most of the cobalt remains within the aggregates. This is expected because no long-range diffusion of cobalt is expected under the reduction conditions. Therefore, with regard to the distribution of the cobalt oxide particles in the alumina pores,^[12,13] no significant changes in the size of the whole aggregate occur through the reduction. Measurements on the cobalt aggregates after reduction give an average of 145 ± 40 nm, which is close to the 158 ± 30 nm for cobalt oxide aggregates.

As described above, while no meaningful TEM particle size can be measured in the oxide aggregates, shrinkage of the Co-phase during reduction leads to separation of the continuous aggregate into an assembly of separate, non-continuous, metallic cobalt particles. Furthermore, the parallel orientation of the continuous Co_3O_4 aggregate is lost during reduction. This is also clearly observed in the results from electron tomography. The 3D structure shows that the metallic cobalt nanoparticles do not have regular shape and their shapes are influenced by the alumina pores.

The particle size measurements from bright field images of the type shown in Figure 4b give an average of 10.0 ± 2.4 nm. The distribution of the cobalt particle sizes indicates that most of them are in the range of 8–14 nm, Figure 5f. By contrast, the measurements on the crystallites in the dark field images of the reduced material, such as Figure 5b, give an average of 7.5 ± 2.5 nm and most have a in the range between 5–9 nm. The particle sizes measured from the bright field images are significantly larger than the crystallite size measured in the dark field images. The contrast of the bright field images makes individual cobalt particles difficult to distinguish relative to the contrast in the dark field images.

Smaller particles in the dark field images may be missed, while faults and grain boundaries reduce the dark field crystallite size relative to the physical particle size seen in the bright field images. This is illustrated in Figure 5d and 5e.

The volume weighted crystallite average value from TEM, 7.5 ± 2.5 nm, is in agreement with the results from the in-situ XRD value of 5 ± 1 nm. This is expected to be underestimated when calculated by XRD, due to the multi-crystalline nature of the particles. From the catalytic point of view, the cobalt particle size defines the surface area for the catalytic reaction which is more accurately obtained by bright field TEM. This illustrates the importance of combining TEM techniques with XRD.

The bright field TEM particle size (10.0 ± 2.4 nm) is comparable with particle size measurements from H_2 Chemisorption (10.2 nm) as it measures the adsorption of H_2 into active surface areas.

Structure of the Catalyst

Cobalt Oxide Structure

As described in our earlier work^[13,15] TEM clearly shows that the Co_3O_4 aggregates contain mosaic structures with a single main crystallographic orientation and a porous morphology that is fully inter-grown with the substrate, as shown in Figures 2c and 4a. This is confirmed by both diffraction and dark field imaging. This ordered crystal structure of the cobalt oxide aggregate can be related to the preparation method, where the cobalt precursor is added to the alumina substrate and precipitated as $\text{Co}(\text{NO}_3)_2 \cdot 6\text{H}_2\text{O}$ in the alumina pores, dried and then calcined. The drying and calcination of the cobalt phase droplets form crystallites of Co_3O_4 and nucleation of this phase proceeds predominantly from a single nucleus that defines the orientation of the final aggregate

Metallic Cobalt Structure

Our previous work on the reduction of cobalt oxide supported on $\alpha\text{-Al}_2\text{O}_3$ by environmental TEM illustrated that the reduction mechanism proceeds through the volume shrinkage of the oxide phase and formation of metallic cobalt.^[11] More recent analysis of those data showed the presence of CoO during transition of Co_3O_4 to Co, which was not recognized in our previous report. TEM investigations of the current sample confirm the shrinkage of particles during reduction. The important point is that only three-dimensional shrinkage occurs through reduction, with separation of the continuous oxide network aggregates into separate metallic nanoparticles. The TEM analysis identified both fcc and hcp cobalt in the catalyst. As observed previously,^[11] smaller particles have fcc structure, while the larger particles mainly have hcp structure. The formation of bulk fcc structure at this temperature is not expected from the thermodynamic point of view. However, the fcc structure may be stabilized kinetically by the fact that the two oxide phases present during reduction are also cubic and the cubic symmetry is maintained during the simple shrinkage of the unit cell as oxygen atoms are eliminated from the structure. A previous XRD study shows the intergrowth of both fcc/hcp structures in the catalyst material which is in accordance with our observation.^[32]

As discussed in the introduction, at ambient temperature, the structure of cobalt nanoparticles is known to be dependent on their size. Kitakami et al.^[12] studied fine cobalt particles synthesized by sputtering and they indicated that the total free energy of the fcc cobalt nanoparticles is lower than the hcp cobalt structure for particles smaller than 20 nm. For particles larger than 40 nm, the hcp structure, with inclusion of very small amounts of fcc, was found to have lower free energy and hence be more stable. In the present study, the cobalt catalyst particle size distribution is mainly below 20 nm, constrained by the alumina pores. The reduction temperature (400 °C) in this study is lower than the bulk transition temperature of the cobalt hcp to fcc (420 °C).

The existence of both fcc and hcp structures in the reduced material for a lower range of particle sizes might also be influenced by the interface between the substrate and the cobalt nanoparticles are attached.

Defects in Metallic Cobalt

The TEM results show a high density of structural defects in both fcc and hcp metallic cobalt nanoparticles as seen in Figure 7. Twinning, edge dislocation, stacking faults, and hcp lamellae were observed. Significant amounts of planar defects occurring during diffusionless martensitic transformation of cobalt has been observed.^[33] The fcc to hcp transformation in cobalt has been described by several authors.^[8,29,34] This can occur by two mechanisms: either by twinning in the fcc structure or by transformation of fcc to hcp by the movement of partial dislocations with Burgers vector of $1/6[112]$.^[29]

Characterizing the planar defects and fcc/hcp lamellae by systematic alignment of individual nanoparticles in the TEM is demanding for particles in a support. Individual nanoparticles are also likely to contain planar defects on crystallographically equivalent planes, producing complex image contrast. Furthermore, the dispersion sample preparation method used to prepare the TEM samples of reduced material, produces irregular sample thicknesses with large overlap of the particles and the support and it did not prove possible to perform a thorough analysis of the planar defects.

It has not been possible to follow the reduction process directly in TEM and the results presented show the microstructure after reduction. It is suggested that reduction initially leads to the formation of fcc cobalt, as this requires the minimum rearrangement of atoms as the fcc CoO is reduced. The hcp cobalt particles and lamellae then form in the metallic state. In order to clarify this structural change sequence, a single crystal particle model during its reduction may be considered where a part of CoO in the middle is surrounded by the cobalt metal. The direct transformation from CoO with fcc structure to the hcp cobalt structure requires the movement of the atomic planes while a portion of the cobalt atoms in these planes are still bonded strongly with the oxygen atoms and their movement is difficult.

In contrast, the change from the fcc CoO to the fcc cobalt structure is energetically more favourable. In this case, the hcp cobalt nanoparticles will have gone through a martensitic transformation of fcc to hcp, leaving a high proportion of faults in their structure.

The formation of the hcp structure from fcc by diffusion is not considered to be significant in the catalysts due to the low process temperatures and small cobalt self-diffusion coefficients. For instance, the self-diffusion coefficient of cobalt based on the reported diffusion coefficients is $3.75 \times 10^{-22} \text{ cm}^2/\text{s}$ at 400°C , considering the temperature dependency of the diffusion coefficient.^[35,36,37] This indicates that the phase transformation of cobalt from fcc to hcp by atomic diffusion and re-ordering of the atomic planes is slow.

The behaviour of the catalyst materials in the FT process may be affected by the structural changes of the metallic cobalt and in particular the existence of defects. It is possible that the catalyst activity is decreased during the recovery of the regular structure (removal of crystal defects) due to operation for a long time at the process temperature (ca. 220°C).

Conclusion

Fischer-Tropsch 20wt%Co/0.5wt%Re/ γ - Al_2O_3 catalyst have been studied by TEM and XRD, before and after reduction. Size, phase and structure characteristics of the oxide and metallic states were characterized.

For the calcined material, cobalt aggregates with an average size of $158 \pm 3 \text{ nm}$ were observed by TEM. These form a continuous, oriented, mosaic network inter-grown with the substrate, as described in earlier work. The average size of the Co_3O_4 crystallites in these aggregates, according to XRD, is $13.2 \pm 1 \text{ nm}$.

The aggregate size does not change significantly on reduction. However, the volume of the cobalt phase decreases and the aggregates separate into distinct particles so that accurate particle size measurement of metallic cobalt nanoparticles is possible. An average particle size of $10.0 \pm 2.4 \text{ nm}$ was measured by bright-field TEM, which is a good match with the particle size obtained from H_2 chemisorption. Dark field imaging of the metallic cobalt nanoparticles gives an average volume weighted crystallite size of $7.5 \pm 2.5 \text{ nm}$, which is slightly larger than the value of $5 \pm 1 \text{ nm}$ obtained by XRD. This is attributed to the existence of defects in the, such as twins, faults. While fcc was observed to be the dominant structure in the metallic cobalt, as expected from XRD, a small proportion of larger particles were found to be hcp cobalt. Significant levels of planar faults associated with the fcc to hcp transformation are observed. Both hcp lamellae in fcc Co particles and fcc lamellae in large hcp particles were observed directly. These faults were reported in earlier XRD studies. The faulting is associated with steps on the surface of cobalt nanoparticles that may influence the catalytic properties by increasing steps density against low index surfaces. Detailed analysis of the individual nanoparticles is challenging due to contrast arising from overlapping faults.

Electron tomography of the reduced catalyst has shown the separation of the cobalt nanoparticles from continuous oxide in the aggregates, due to shrinkage during reduction. The 3D analysis suggests that the shape of the metallic cobalt particles is influenced by the shape of the alumina support pores. The metallic cobalt crystallites within one reduced aggregate do not have a clear common crystallographic orientation. This may be due to the reduction of cobalt oxide particle from individual nucleation points, and to particle rotation during reduction.

The work shows the value of combining TEM and XRD techniques in order to optimize design and processing based on an understanding the catalyst nanostructure. It also provides a reference for studies of the nanostructure after catalytic reaction.

Experimental Section

The details of the Fischer-Tropsch catalyst preparation and the application of TEM and XRD techniques for its characterization described as follow.

Catalyst Preparation

The FT catalyst was synthesized through one-step incipient wetness impregnation of the alumina support with an aqueous solution of cobalt nitrate hexahydrate, $\text{Co}(\text{NO}_3)_2 \cdot 6\text{H}_2\text{O}$, and perrhenic acid, HReO_4 , to provide a rhenium promoter. The cobalt and rhenium loadings on the $\gamma\text{-Al}_2\text{O}_3$ support were 20 wt% and 0.5 wt%, respectively. The $\gamma\text{-Al}_2\text{O}_3$ pore size was measured through nitrogen adsorption-desorption experiments using the Barrett-Joyner-Halenda (BJH) equation, which gave average value of 11.6 nm for the pore size distribution.^[38] After impregnation, the catalyst was dried at 110 °C for 3 hours and then calcined in air at 300 °C for 16 h to form cobalt oxide particles with a composition 20wt%Co/0.5wt% Re/ $\gamma\text{-Al}_2\text{O}_3$. A ramping rate of 2 °C/min was used to heat the sample from ambient temperature to the final calcination temperature. For TEM, the sample was then reduced with a heating rate of 3 °C/min up to 350 °C under 100 ml/min H_2 flow at ambient pressure and then kept for 16 h under these conditions.

For comparison, results from non-promoted catalyst are also presented. This sample was prepared through the same route, except that HReO_4 was not added to the precursor and the final composition was 20wt%Co/ $\gamma\text{-Al}_2\text{O}_3$. A batch of substrate was also exposed to the same heating and calcination steps without addition of any precursor. Reduction conditions for XRD are described later in this section.

TEM

TEM experiments were performed using Philips CM30 with a LaB_6 filament and JEOL 2010F with a field emission gun, both operated at 200 kV accelerating voltage. TEM samples of the non-reduced material were prepared by ultramicrotomy. In this technique, a small amount of catalyst powder was embedded in a resin and stored overnight at ambient temperature. Thin uniform slices were then obtained by cutting the embedded catalyst with a diamond blade, using a commercial ultramicrotome. The slices were collected on a carbon supported Cu mesh grid. TEM samples of the reduced material were prepared by dispersion of the crushed catalysts powder on a carbon supported Cu mesh grid inside a glove box. The reduced TEM sample was transferred from the glove box to the TEM using a TEM holder protected from the air by a TEM holder cap. The cap was removed inside a glove bag, which was connected to the TEM goniometer, while it was flushed with Argon gas, as the holder was introduced into the goniometer. TEM data analysis was performed with Digital Micrograph and Process Diffraction software.^[39,40] TEM particle size measurements were performed by direct measurements on the TEM images using Digital Micrograph tools.

Electron tomography was also applied to obtain detail information on the three-dimensional structure of the reduced catalyst. Electron tomography was performed in Scanning TEM (STEM) mode in the tilt range of ± 72 degree. Alignment and reconstruction were performed with Digital Micrograph software. The visualization was done using Avizo 6.2, software from Visualization Science Group.

XRD

The catalyst was characterized by High-resolution X-ray powder diffraction (HR-XRD) before and after reduction. The measurements were performed at the BM01B station of the Swiss-Norwegian Beamlines (SNBL). The X-ray beam was adjusted with the use of a Si (1-1-1) monochromators to the energy of 24.698 eV, corresponding to a wavelength of 0.502 Å. The applied slits provided an X-ray beam spot of 4 mm horizontal size and 1 mm vertical size at the sample position. The diffractometer is equipped with an X-ray detector consisting of six independent counting chains, each made of the Si (1-1-1) analyser crystal and a NaI scintillation counter. Data were collected in the 2θ range from 9° to 33° before and after reduction.

Catalyst reduction was done in-situ at 400 °C and under 2.5 ml/min pure H_2 flow. In particular, 7–10 mg of the sample was loaded into a quartz capillary 1-mm in diameter and the sample was kept in place by quartz wool plugs. The cell design and experimental set up is described in detail elsewhere.^[14, 22] The sample was heated from ambient temperature to 400 °C at a rate of 3 °C/min at ambient pressure. When the desired set point was reached, the temperature was held for 4 h before switching to a He flow of 5 ml/min and ramp down to room temperature.

Data analysis was done using Topas v4.2 software. This provided both structural and crystallite size information. For the full profile fitting, decomposition of the diffraction patterns has been done by the Pawley method.^[41]

Hydrogen Chemisorption

Hydrogen adsorption isotherms performed on a Micromeritics ASAP 2010 unit at 39 °C. The samples were evacuated at 39 °C for 1 h and then reduced in situ in flowing hydrogen at 350 °C for 16 h. The temperature was increased by 1 °C /min from 39 to 350 °C. After reduction, the samples were evacuated at 330 K for 1 h and 30 min at 100 °C before cooling to 39 °C. The adsorption isotherm was recorded in the pressure interval ranging from 20 to 510 mmHg. The amount of adsorbed hydrogen was used to calculate cobalt dispersion and particle size, assuming that two cobalt sites are covered by one hydrogen molecule^[1] and that rhenium does not contribute to the amount of hydrogen adsorbed. The average diameter of metallic cobalt nanoparticles ($d(\text{Co}^0)$, nm) was calculated from the cobalt metal dispersion (D , %) by assuming uniform spherical metal particles with site density of 14.6 at/nm².

Acknowledgements

Financial support from the Research council of Norway and Equinor (previously Statoil) through the KMB project (0169673/S10) are gratefully acknowledged. The financial support from inGAP centre of research-based innovation, supported by the Norwegian research council under contract no. 174893 is greatly acknowledged. Prof. Jafar Safarian at NTNU is greatly acknowledged for his invaluable scientific discussions, as well as the Swiss-Norwegian Beamlines personnel for assistance during experiment 01-01-850.

Conflict of Interest

The authors declare no conflict of interest.

Data Availability Statement

The data that support the findings of this study are available from the corresponding author upon reasonable request.

Keywords: Cobalt catalyst · Fischer-Tropsch · Reduction · Transmission electron microscopy · X-ray diffraction

- [1] A. Y. Khodakov, W. Chu, P. Fongarland, *Chem. Rev.* **2007**, *107*, 1692–1744.
- [2] E. Iglesia, S. L. Soled, R. A. Fiato, *J. Catal.* **1992**, *137*, 212–224.
- [3] P. Li, J. Liu, N. Nag, P. A. Crozier, *Appl. Catal. A* **2006**, *307*, 212–221.
- [4] D. Ozkaya, M. Lok, J. Casci, P. Ash, *Sapporo* **2006**, *3*, 1561.
- [5] W. L. Smith, A. D. Hobson, *Acta Crystallogr.* **1973**, *B29*, 362.
- [6] Powder diffraction file, Inorganic phases, International centre for diffraction data, **1986**, pp. 538 and 532.
- [7] N. E. Tsakoumis, et al., *Chem. Commun.* **2016**, *52*, 3239–3242.
- [8] A. R. Troiano, J. L. Tokich, *Trans. Am. Inst. Min. Eng.* **1948**, *175*, 728–741.
- [9] O. Ducreux, B. Rebours, J. Lynch, M. Roy-Auberger, D. Bazin, *Oil Gas Sci. Technol. - Rev. IFP.* **2009**, *64*, 49–62.
- [10] O. A. Bulavchenko, S. V. Cherepanova, V. V. Malakhov, L. S. Dovlitova, A. V. Ishchenko, S. V. Tsybulya, *Kinet.Catal.* **2009**, *50*, 192–198.
- [11] R. Dehghan, T. W. Hansen, J. B. Wagner, A. Holmen, E. Rytter, Ø Borg, J. C. Walmsley, *Catal. Lett.* **2011**, *141*, 754–761; Borg, J. C. Walmsley, *Catal. Lett.* **2011**, *141*, 754–761.
- [12] O. Kitakami, H. Sato, Y. Shimada, *Phys. Rev. B*, **1997**, *56*, 21, 13849–13854.
- [13] Ø. Borg, J. C. Walmsley, R. Dehghan, B. S. Tanem, E. A. Blekkan, S. Eri, E. Rytter, A. Holmen, *Catal. Lett.* **2008**, *126*, 224–230.
- [14] M. Rønning, N. E. Tsakoumis, A. Voronov, R. E. Johnsen, P. Norby, W. van Beek, Ø. Borg, E. Rytter, A. Holmen, *Catal. Today* **2010**, *155*, 3–4, 289–295.
- [15] I. Arslan, J. C. Walmsley, E. Rytter, E. Bergene, P. Midgley, *J. Am. Chem. Soc.* **2008**, *130*, 5716–5719.
- [16] E. Rytter, N. E. Tsakoumis, A. Holmen, *Catal. Today* **2016**, *261*, 3–16.
- [17] Ø. Borg, N. Hammer, S. Eri, O. A. Lindvåg, R. Myrstad, E. A. Blekkan, M. Rønning, E. Rytter, A. Holmen, *Catal. Today* **2009**, *142*, 70–77.
- [18] A. M. Hilmen, D. Schanke, A. Holmen, *Catal. Lett.* **1996**, *38*, 143–147.
- [19] A. Voronov, N. E. Tsakoumis, N. Hammer, W. Van Beek, H. Emerich, M. Rønning, *Catal. Today* **2014**, *229*, 23–33.
- [20] C. M. Andrei, J. C. Walmsley, H. W. Brinks, R. Holmestad, S. S. Srinivasan, C. M. Jensen, B. C. Hauback, *Appl. Phys. A* **2005**, *80*, 709–715.
- [21] L. Braconnier, E. Landrison, I. Clemenccon, C. Legens, F. Diehl, Y. Schuurman, *Catal. Today* **2013**, *215*, 18–23.
- [22] N. E. Tsakoumis, A. Voronov, M. Rønning, W. van Beek, Ø. Borg, E. Rytter, A. Holmen, *J. Catal.* **2012**, *291*, 138–148.
- [23] E. Patanou, N. E. Tsakoumis, R. Myrstad, E. A. Blekkan, *Appl. Catal. A* **2018**, *549*, 280–288.
- [24] S. J. Andersen, B. Holme, C. D. Marioara, *Ultramicroscopy* **2008**, *108*, 750–762.
- [25] D. B. Williams, C. B. Carter, Transmission electron microscopy, Plenum press, New York, **1996**.
- [26] B. Yao, T. Sun, A. Warren, H. Heinrich, K. Barmak, K. R. Coffey, *Micron* **2010**, *41*, 177–182.
- [27] N. E. Tsakoumis, J. C. Walmsley, M. Rønning, W. V. Beek, E. Rytter, A. Holmen, *J. Am. Chem. Soc.* **2017**, *139*, 3706–3715.
- [28] M. Beier, T. Hansen, J. Grunwaldt, *J. Catal.* **2009**, *266*, 2, 320–330.
- [29] R. Reuel, C. H. Bartholomew, *J. Catal.* **1984**, *77*, 63–77.
- [30] E. Rytter, Ø. Borg, N. E. Tsakoumis, A. Holmen, *J. Catal.* **2018**, *365*, 334–343.
- [31] Ø. Borg, S. Eri, S. Storsæter, E. A. Blekkan, H. Wigum, E. Rytter, A. Holmen, *J. Catal.* **2007**, *248*, 89.
- [32] N. E. Tsakoumis, R. Dehghan-Niri, M. Rønning, J. C. Walmsley, Ø. Borg, E. Rytter, A. Holmen, *Appl. Catal. A* **2014**, *479*, 59–69.
- [33] J. W. Christian, The theory of the transformation in metals and alloys, Pergamon Press, First Edition, **1965**.
- [34] P. G. Shewmon, Transformations in metals, McGraw-Hill Book Company, **1969**.
- [35] F. C. Nix, F. E. Jaumot Jr. *Phys. Rev.* **1951**, *82*, 72–74.
- [36] K. Hirano, R. P. Agarwala, B. L. Averbach, M. Cohen, *Appl. Phys.* **1962**, *33*, 3049–3054.
- [37] J. J. B. Prasad, K. V. Reddy, *Bull. Mater. Sci.* **1985**, *7*, 15–20.
- [38] E. P. Barrett, L. G. Joyner, P. P. Halenda, *J. Am. Chem. Soc.* **1951**, *73* 373–380.
- [39] D. R. G. Mitchell, B. Schaffer, *Ultramicroscopy* **2005**, *103*, 319–332.
- [40] J. L. Labar, *Ultramicroscopy* **2005**, *103*, 237–249.
- [41] G. S. Pawley, *J. Appl. Crystallogr.* **1981**, *14*, 357–361.

Manuscript received: January 3, 2022
Revised manuscript received: February 28, 2022
Accepted manuscript online: March 11, 2022
Version of record online: May 4, 2022